

Three-dimensional assessment of low velocity impact damage in particle toughened composite laminates using micro-focus X-ray computed tomography and synchrotron radiation laminography

D.J. Bull^{1*}, S.M. Spearing¹, I. Sinclair¹, L. Helfen^{2,3},

¹ Materials Research Group, Faculty of Engineering and the Environment, University of Southampton, Southampton, United Kingdom

² ANKA / Institute for Synchrotron Radiation, Karlsruhe Institute of Technology, Karlsruhe, Germany

³ European Synchrotron Radiation Facility (ESRF), 6 rue Jules Horowitz, Grenoble, France

*Corresponding author: daniel.bull@soton.ac.uk

Abstract

Results are presented studying the contribution of particle toughening to impact damage resistance in carbon fibre reinforced polymer materials. Micro-focus X-ray computed tomography and synchrotron radiation computed laminography were used to provide a novel, multiscale approach for assessing impact damage. Thin (1mm thick) composite plates containing either untoughened or particle-toughened resin systems were subjected to low velocity impact.

Damage was assessed three-dimensionally at voxel resolutions of 0.7 μm and 4.3 μm using SRCL and μCT respectively; the former being an innovative approach to the laterally extended geometry of CFRP plates. Observations and measurements taken from μCT scans captured the full extent of impact damage on both material systems revealing an interconnected network of intra- and inter-laminar cracks. These lower resolution images reveal that the particle-toughened system suppresses delaminations with little effect on intralaminar

damage. The higher resolution images reveal that the particles contribute to toughening by crack deflection and bridging.

Keywords: A. carbon fibre; B. impact behaviour; B. toughness; X-ray computed tomography

1 Introduction

Carbon fibre reinforced polymer (CFRP) composites are susceptible to low velocity impact that can create internal damage barely visible at the surface. This damage, in particular interlaminar delaminations, has been widely reported to have a deleterious effect on the residual in-plane compression after impact (CAI) strength of the material e.g. [1]. The projected delamination area is known to correlate with residual CAI strength [2]; therefore toughening the material to increase damage resistance is desirable.

It has been shown that the inclusion of thermoplastic toughening particles in the resin of carbon fibre composites can lead to improved toughness in simple delamination fracture tests [3]. The mechanisms of particle-toughening include: crack deflection, crack bridging, crack-tip blunting, particle-matrix interface debonding, and particle-induced localised yielding [2, 4-9]. Whilst these toughening micromechanisms are understood, it is less clear as to what toughening mechanisms are present in particular systems and their relative contributions to the overall toughness. Additionally, it is less clear how such toughening strategies translate to the more complicated damage state associated with impact loading. This is exacerbated by the more commonly used techniques for impact damage characterisation which typically yield two-

dimensional information; e.g. ultrasonic C-scan or cross-sectional microscopy. These obscure the three-dimensionality of the interacting damage modes associated with composite impact.

To accommodate the three-dimensional (3D) characteristics of impact damage and to study particle toughening micromechanisms, micro-focus computed tomography (μ CT) [10] and synchrotron radiation computed laminography (SRCL) [11] using propagation-based phase contrast [12, 13] have been used in this study. The combination of SRCL and laboratory μ CT imaging methods allow the effects of particle toughening to be observed at microscopic and mesoscopic levels at routinely achievable voxel resolutions with each of the two imaging techniques. This is of the order of $>2\text{-}3\ \mu\text{m}$ for μ CT, and $<1\ \mu\text{m}$ for synchrotron radiation imaging methods. A comparison of these 3D imaging techniques is described in a previous study on CFRP materials subjected to low velocity impact [14].

μ CT has been used in previous studies to assess internal damage in composites at meso- and macroscopic scales [15-23]; however due to the use of relatively thin rectangular composite plates as impact test coupons, this leads to large variations in X-ray path length during the rotation of the scan. Typically specimens are cut to form 'matchsticks' with cross-sections of a few mm^2 [19, 24] to achieve the best quality scans, but this is destructive and introduces the likelihood of cutting artefacts distorting the observed damage. SRCL, a technique better suited to laterally extended geometries [12, 25] including sheet or panel like material specimens [26, 27], offers non-destructive, μm -scale

imaging of damage micromechanisms at local regions, without machining the specimen to a reduced cross-section [26, 28]. Unlike traditional, higher resolution methods such as cross-sectional microscopy, the non-destructive nature of SRCL ensures that damage post-impact is unaffected by cutting artefacts, polishing, *etc.* increasing confidence in the observations.

Computed laminography is essentially similar to computed tomography, however instead of the axis of rotation being perpendicular to the incident beam, it is inclined at an angle minimising the large variation in X-ray path length on laterally extended objects. A schematic of the setup can be found in [14]. This inclination however does lead to artefacts in the reconstructed 3D data due to incomplete sampling of the Fourier-space [14] but often these artefacts are less disruptive than corresponding artefacts of limited-angle μ CT [29, 30]. The details of the operation and assessments of the capabilities and limitations of SRCL imaging for composite materials can be found in previous studies [25, 26, 28]. The advantage of 3D imaging *via* SRCL is that the flat specimen can stay intact and any ROI on the plate-like specimen can be imaged at high resolution without sample extraction. Moreover, due to the non-destructive nature of the technique, the specimen can be scanned laterally and the 3D images of different scans concatenated afterwards [28]. A different approach is to displace the rotation axis in order to concatenate projections before the image reconstruction step [7] to emulate a larger detector with the same spatial resolution.

In this work these imaging techniques are combined to offer a multiscale damage assessment of particle-toughened and untoughened systems subjected to low velocity impact.

2 Materials and methods

2.1 Materials

The materials tested in the present study consisted of unidirectional carbon fibre prepreg material with an 8 ply quasi-isotropic $[45, 0, -45, 90]_s$ layup. Two materials were used, encompassing proprietary particle-toughened and an untoughened matrix system (Cytac Engineered Materials Ltd), the former incorporating thermoplastic particles within the epoxy matrix that were concentrated at the interface of the prepreg. For direct comparison, the untoughened system used the same intermediate modulus carbon fibre and base resin as the particle-toughened system and the same fibre to matrix (resin plus particles) ratio by weight were used. Plates were laid up and cured in an autoclave, using an aerospace industry-standard cure cycle, before being cut to 80 x 80 *mm* test coupons. The thickness of the cured material was approximately 1 *mm*. This thickness of material was chosen as it was known to work with previous laminography studies at the time [26].

2.2 Impact testing

Coupons were impacted on an impact drop tower using a 16 *mm* hemispherical tup with a 4.9 *kg* mass. The coupons were attached to a base plate with a 60 *mm* diameter ring as carried out in [31]. The drop height determined the impact energy used and a single strike mechanism prevented multiple impacts. To aid

like-for-like comparison of microscopic and macroscopic behaviour in untoughened and particle-toughened systems, impact conditions were selected for an equivalent nominal projected damage area (approximately 50 mm^2 , as measured by ultrasonic C-scan to result in a 4 mm damage radius that could be captured within relatively few CT scans). Ultrasonic C-scan measurements had an XY resolution of 1 mm .

Specimens were impacted at a range of impact energies between 0.3 J and 3.0 J , see Figure 1, with impact energies of 0.6 J and 1.2 J being identified for the non-particle and particle toughened coupons respectively to achieve the desired projected damage area (*i.e.* $\sim 50 \text{ mm}^2$), although it should be noted that there is some scatter in the data as indicated by the 95% prediction intervals. The damage areas exhibited by the particle toughened system are clearly reduced in comparison to the untoughened sample tests. This is progressively more evident at impact energies of 2 J and above; corresponding to the increasing prevalence of delamination in the untoughened material at higher impact energies.

2.3 μ CT and SRCL procedure

Post-impacted specimens were prepared for damage assessment by μ CT and SRCL. Separate specimens were used for μ CT and SRCL studies. μ CT studies were performed on the material systems first to better understand the damage formation and identify regions of interest for SRCL work. In both techniques the coupons studied consisted of an untoughened and toughened system impacted at 0.6 J and 1.2 J respectively.

For SRCL studies, local regions within complete impacted coupons were scanned at four locations, as shown in Figure 2, for both an untoughened and toughened system. Each scanned region consisted of a volume with a field of view measuring approximately $1 \times 1 \times 1 \text{ mm}$ at a voxel resolution of $0.7 \mu\text{m}$. The relatively small field of view is a trade-off with the high voxel resolution used in this study but could be extended by the techniques mentioned in the introduction [7, 28]. A monochromatic beam with an energy of 19 kV was used with an exposure time of 100 ms over 1500 projections. Local regions of interest (ROIs) were located via the fluorescence arising from a glass coverslip attached to the surface of the coupon. As such, a precise location of the beam was achieved for ROI assessment of the samples. Once positioned, the coverslip was removed from the coupon surface prior to scanning. Scanning of region 'A' (Figure 2) was undertaken at the impact site determined from the centre of the coupon. Scanning of regions 'B-D' was carried out 2 to 4 mm up from the impact site to ensure the edge of the damage area would be captured. Each scan took approximately 15 minutes, however beamtime constraints and lengthy changeover periods (~15 minutes per scan location, ~60 minutes per specimen changeover) restricted this study to focus on one toughened and one untoughened coupon of equivalent nominal projected damage area at the four regions described.

Preparation of coupons for μCT studies are shown in a schematic in Figure 3. Four "matchstick" strips measuring approximately 4 mm wide were cut across the damage area. These were stacked back to back to form a combined 'matchstick' with a cross-section approximately $4 \times 4 \text{ mm}$. This stack was

scanned on a Nikon Metrology HMX 225 CT scanner at three locations along the length of the 'matchstick' to capture the entire damage extent. A Molybdenum target with no filtering and a beam energy of 65 kV and 70 μ A was used. An exposure time of 2 seconds over 2000 projections averaged over two frames per projection led to a scan time approximately 2.5 hours.

Whilst the μ CT analysis in this case involved sub-sectioning of specimens for moderate voxel resolution imaging (4.3 μ m) of the overall damage, it should be recognised that by using synchrotron laminography a non-destructive high resolution analysis, can be performed where associated micromechanical observations are attributable to low-velocity impact processes alone.

Segmentation and realignment of the image volumes obtained from multiple μ CT scans was carried out using VG Studio Max 2.1TM software. Due to the width of the blade used to cut the "matchsticks", 0.3 mm wide strips are missing between adjacent "matchsticks".

3 Results and discussion

3.1 Impact damage mechanisms observed from μ CT

A cross-sectional slice obtained from μ CT is shown in Figure 4 for both material systems. A cone of internal damage is revealed at the impact region containing commonly observed modes of damage: (i) shear induced matrix cracks, (ii) delaminations and (iii) bending induced tensile matrix cracks towards the back

face [32, 33]. Some evidence of delamination crack ligamented behaviour in the toughened system is observed in (iv).

Segmentation of all detectable impact damage obtained from μ CT scans revealed the 3D impact damage morphology and is shown in Figure 5. Based on previous observations, the crack opening detectability limit of cracks was taken to be approximately 30% of the voxel resolution used (*i.e.* just over $1 \mu\text{m}$ in this case) [14]. Due to the method of cutting ‘matchsticks’, some information representative of the width of the 0.3 mm blade is absent; despite this limitation, the overall internal 3D damage structure can be identified. A colour key is shown where blue represents the presence of delamination and each of the other colours represents intralaminar damage occurring on that particular ply. For clarity, the delaminations are labelled in Figure 5 i-iv at the 7/8, 6/7, 5/6 and 5/6 ply interface respectively. In both material systems, a similar damage interaction and morphology is observed on this scale. A characteristic “cone” of impact damage is formed around the impact site, consisting of a network of delaminations interlinked by intralaminar matrix cracks. These intralaminar matrix cracks occur parallel to the direction of the fibres and form at tangents to a concentric ring surrounding the impact site. This leads to a “spiral staircase” of delaminations consisting of 45° segments that form between two matrix cracks of different orientations. This is consistent with other studies using quasi-isotropic layups *e.g.* [19, 33]. Delaminations always occur within the boundaries of matrix cracks on plies of different orientation, consistent with initiation of delaminations from critical matrix cracks, *e.g.* see [33].

The extent of the detectable delamination areas was measured at each ply interface and is plotted in Figure 6. The total delamination areas measured by μ CT were typically lower than the projected damage areas measured by ultrasonic C-scan. There are two contributions to this; the 1 mm XY resolution of the C-scan has overestimated the damage area by including damage beneath the impact cone. This is likely due to the ultrasonic probe partially detecting neighbouring cracks at these locations. Secondly, the detectability of cracks was limited to crack openings above $\sim 30\%$ of the voxel resolution; this typically underestimates the true extent of the damage areas and crack lengths. Nonetheless, relative comparisons to the extent of detectable damage between the two material systems can be made.

Delaminations in this study were observed occurring dominantly at the rear three ply interfaces below the mid-plane on both the untoughened and toughened systems, although some delamination was also observed above the mid-plane in the untoughened system. It is probable that a combination of the Hertzian cone stress field due to the point impact load and bending stresses contributed to a greater incidence of damage on the lower half of the material.

Toughening particles constrained delaminations and in this particular case, measurement of delamination areas taken from μ CT data when plotted in Figure 6 show that the toughened coupon resulted in a lower extent of delaminations across all ply interfaces despite the higher impact energy.

Observations in Figure 5 near the outer tips of delaminations in the toughened system show discontinuities in the crack which are attributed to particle toughening behaviour.

The incidence of intralaminar cracks did not appear to be equivalently controlled as delaminations in the toughened system. Intralaminar crack lengths were measured from the μ CT data and plotted in Figure 7 for both systems, for clarity these are plotted on two separate scatter plots. Despite the lower level of delaminations, there is a significantly greater intralaminar crack density, although crack lengths are of similar lengths. It is possible that particle toughening is most effective at the interlaminar regions between plies, consistent with the particles being constrained to these regions [34].

3.2 SRCL observation of toughening micromechanisms

To identify the micromechanisms of particle toughening, higher resolution SRCL scans were utilised. As noted in the introduction, the non-destructive nature of this technique increases the confidence that the observed damage micromechanisms were solely caused by the impact event.

Figure 8 shows a 3D segmentation of matrix and delamination cracks at regions 'A to D' (see Figure 2) on both the untoughened and toughened system as viewed at an angle towards the back face of the coupon. Whilst exact centering of the Region 'A' scans at the mid-point of the impacts was compromised in this case by slight experimental error, ultrasonic C-scan confirmed that the ROIs in Region 'C' captured the delamination edge regions in both materials, whilst the tips of intralaminar cracks were captured in Region 'D'.

To understand the role particle toughening plays, cross-sectional slices from SRCL data are shown in Figure 9. Similarly to the μ CT cross-sections, key

damage features consist of (i) delaminations and (ii) intralaminar cracks. However an additional level of detail is revealed, the untoughened and particle toughened systems show distinct differences in the delamination micromechanisms and the presence of an approximately $20\ \mu\text{m}$ thick resin-rich region (Figure 9(iii)) in the particle toughened system. Although toughening particles cannot be directly visualised in the present scan data due to the particles being chemically closely related to the resin (in contrast to observations made on a different particle composition in a previous study with particle sizes in the order of the same magnitude [34]); it is probable particles may have induced both crack deflection and crack bridging which are clearly visible (Figure 9(iv)). The resulting ligamented behaviour of the delamination is consistent with crack deflection at the crack tip and subsequent bridging in the wake. Spacing of the order of $\sim 20\text{-}80\ \mu\text{m}$ is observed between crack segments. In comparison, delamination cracking in the untoughened system is restricted to narrow deflections on the order of a few fibres diameters, $< 14\ \mu\text{m}$. Such crack shielding and bridging mechanisms within the particle-containing matrix are consistent with reducing delamination propagation: bridging creates traction between plies, reducing the stresses at the crack tip [35], whilst crack deflection reduces the crack-tip stress intensity factor and increase the effective crack area [2]. These processes may act in conjunction with an increased process zone volume associated with the resin rich-layer [36], allowing greater energy absorption with crack propagation [5, 37, 38].

In both material cases, the delamination crack ligaments are oriented at an angles in the range $30^\circ\text{-}45^\circ$ to the plane of the plies indicating their micro-scale

formation is controlled by a combination of tensile and shear stresses; similar observations are made in [39]. Macroscopically the delaminations under low velocity impact conditions propagate in shear due to bending stresses, which is also consistent with earlier observations [32, 33].

In the untoughened system, some local resin-rich regions ($> 10 \mu\text{m}$ thickness) were present between ply interfaces as shown in Figure 10(i). These were typically less than 5% of the total interface surface area. This led to cracks with local deflections of similar orders to the toughened material. Such resin-rich variations during the manufacturing process will affect the local effective toughness and may be anticipated to contribute to variability in the impact response.

SRCL cross-sectional images taken from the edge of the impact damage region in Figure 11 (Region 'C') reveals similar delamination micromechanisms as observed near the impact site, albeit with smaller crack-openings. This consists again of crack deflections on the order of a few fibre diameters (i) in the untoughened system and larger scale crack deflection and bridging (ii) in the toughened system, demonstrating toughening micromechanisms occurring throughout the damaged area.

Some fibre-resin debonding was observed in Figure 11 (ii) between the -45° and 90° in the toughened system, similar behaviour is also shown in Figure 10 (ii) in the untoughened material system. The observed frequency of this behaviour was less than 1% of the total delamination area in the toughened material system and is therefore anticipated to have little effect on the key

toughening mechanisms discussed or the macroscale response. For the untoughened system, the lack of a thick resin-rich region made this observation difficult to distinguish from microcracking and could only be detected unambiguously in thick resin-rich areas ($> 10 \mu m$ thick).

4 Discussion and conclusions

The μ CT and SRCL techniques have been applied to provide novel 3D insights as to the micro-mechanical damage mechanisms responsible for impact damage resistance in CFRP materials. The particle-toughened system tested exhibited clear improvements in delamination growth resistance where delamination suppression is critical to retaining post-impact compression strength.. Toughening clearly induces extensive crack deflection and crack bridging within $\sim 20 \mu m$ thick interlaminar resin-rich regions, which contain the great majority of toughening particles. Delaminations in the untoughened system were relatively planar, with little or no bridging, being constrained to local deflections of the order of a few fibre diameters within the relatively thin interlaminar region.

It is probable the presence of particles at the interlaminar region is highly effective at suppressing delaminations, but less so with intralaminar matrix cracks. Despite a larger impact energy used, the toughened system resulted in a lower extent of detectable delaminations in the μ CT scans, however the lengths of intralaminar cracks were similar compared to the untoughened system. Further study comparing both systems impacted at the same energy would be required to confirm the influence of particles on matrix cracks. Such

ineffectiveness of interlaminar particle toughening to reduce intralaminar damage may be identified as a weakness in cases where water ingress [40] or post-impact fatigue damage growth [41] are of concern.

Overall the work presented in this paper highlights the potential for the use of complementary, multi-scale, 3D X-ray scanning methods to relate the micromechanical damage behaviour to the macroscopic mechanical responses of composite materials and structures.

Acknowledgements

The authors wish to thank the ESRF for beamtime at beamline ID19 and Tilo Baumbach for his investment in the development of this technique. Thanks to μ -VIS at the University of Southampton for use of μ CT and computer suite facilities. μ VIS was enabled by funding from the Engineering and Physical Sciences Research Council. The paper also acknowledges Cytec Engineered Materials Ltd for their sponsorship and supply of materials used in this project with thanks to Mr. Sam Hill and Dr. Kingsley Ho for their support as technical points of contact.

References

- [1] de Freitas M, Reis L. Failure mechanisms on composite specimens subjected to compression after impact. *Compos Struct.* 1998;42(4):365-73.
- [2] Reis L, de Freitas M. Damage growth analysis of low velocity impacted composite panels. *Compos Struct.* 1997;38(1-4):509-15.
- [3] Gao F, Jiao GQ, Lu ZX, Ning RC. Mode II delamination and damage resistance of carbon/epoxy composite laminates interleaved with thermoplastic particles. *J Compos Mater.* 2007;41(1):111-23.
- [4] Fu SY, Feng XQ, Lauke B, Mai YW. Effects of particle size, particle/matrix interface adhesion and particle loading on mechanical properties of particulate-polymer composites. *Compos Part B-Eng.* 2008;39(6):933-61.

- [5] Spanoudakis J, Young RJ. Crack-Propagation in a Glass Particle-Filled Epoxy-Resin .2. Effect of Particle Matrix Adhesion. *J Mater Sci.* 1984;19(2):487-96.
- [6] Hsueh CH. Effects of Aspect Ratios of Ellipsoidal Inclusions on Elastic Stress Transfer of Ceramic Composites. *J Am Ceram Soc.* 1989;72(2):344-7.
- [7] Houssaye A, Xu F, Helfen L, De Buffrenil V, Baumbach T, Tafforeau P. Three-Dimensional Pelvis and Limb Anatomy of the Cenomanian Hind-Limbed Snake *Eupodophis Descouensi* (Squamata, Ophidia) Revealed by Synchrotron-Radiation Computed Laminography. *J Vertebr Paleontol.* 2011;31(1):2-7.
- [8] Pearson RA. Toughening Epoxies Using Rigid Thermoplastic Particles - a Review. *Adv Chem Ser.* 1993(233):405-25.
- [9] Spanoudakis J, Young RJ. Crack-Propagation in a Glass Particle-Filled Epoxy-Resin .1. Effect of Particle-Volume Fraction and Size. *J Mater Sci.* 1984;19(2):473-86.
- [10] Flannery BP, Deckman HW, Roberge WG, Damico KL. 3-Dimensional X-Ray Microtomography. *Science.* 1987;237(4821):1439-44.
- [11] Helfen L, Baumbach T, Mikulik P, Kiel D, Pernot P, Cloetens P, et al. High-resolution three-dimensional imaging of flat objects by synchrotron-radiation computed laminography. *Appl Phys Lett.* 2005;86(7).
- [12] Krug K, Porra L, Coan P, Wallert A, Dik J, Coerdts A, et al. Relics in medieval altarpieces? Combining X-ray tomographic, laminographic and phase-contrast imaging to visualize thin organic objects in paintings. *J Synchrotron Radiat.* 2008;15:55-61.
- [13] Helfen L, Baumbach T, Cloetens P, Baruchel J. Phase-contrast and holographic computed laminography. *Appl Phys Lett.* 2009;94(10).
- [14] Bull DJ, Helfen L, Sinclair I, Spearing SM, Baumbach T. A comparison of multi-scale 3D X-ray tomographic inspection techniques for assessing carbon fibre composite impact damage. *Compos Sci Technol.* 2013;75(0):55-61.
- [15] Archer E, King, S, Quinn, JP, Buchanan, S and McIlhagger. Impact damage analysis of 3D woven carbon fibre composites using computed tomography. 18th international conference on composite materials. South Korea: The Korean society for composite materials; 2011. p. 6.
- [16] Bathias C, Cagnasso A. Application of X-Ray Tomography to the Nondestructive Testing of High-Performance Polymer Composites. *Am Soc Test Mater.* 1992;1128:35-54.
- [17] Crupi V, Epasto G, Guglielmino E. Computed Tomography analysis of damage in composites subjected to impact loading. V Crupi et alii, *Frattura ed Integrità Strutturale.* 2011;17:32-41.
- [18] Enfedaque A, Molina-Aldareguia JM, Galvez F, Gonzalez C, Llorca J. Effect of Glass Fiber Hybridization on the Behavior Under Impact of Woven Carbon Fiber/Epoxy Laminates. *J Compos Mater.* 2010;44(25):3051-68.
- [19] McCombe GP, Rouse J, Trask RS, Withers PJ, Bond IP. X-ray damage characterisation in self-healing fibre reinforced polymers. *Compos Part a-Appl S.* 2012;43(4):613-20.
- [20] Pandita SD, Falconet D, Verpoest I. Impact properties of weft knitted fabric reinforced composites. *Compos Sci Technol.* 2002;62(7-8):1113-23.
- [21] Schilling PJ, Karedla BPR, Tatiparthi AK, Verges MA, Herrington PD. X-ray computed microtomography of internal damage in fiber reinforced polymer matrix composites. *Compos Sci Technol.* 2005;65(14):2071-8.
- [22] Sugimoto S, Aoki T, Iwahori Y, Ishikawa T. Nondestructive evaluation of composites using Micro-Focused X-Ray CT Scanner. *Aip Conf Proc.* 2005;760:1081-6.
- [23] Tan KT, Watanabe N, Iwahori Y. X-ray radiography and micro-computed tomography examination of damage characteristics in stitched composites subjected to impact loading. *Compos Part B-Eng.* 2011;42(4):874-84.
- [24] Wright P, Fu X, Sinclair I, Spearing SM. Ultra high resolution computed tomography of damage in notched carbon fiber-epoxy composites. *J Compos Mater.* 2008;42(19):1993-2002.

- [25] Helfen L, Myagotin A, Pernot P, DiMichiel M, Mikulik P, Berthold A, et al. Investigation of hybrid pixel detector arrays by synchrotron-radiation imaging. *Nucl Instrum Meth A*. 2006;563(1):163-6.
- [26] Moffat AJ, Wright P, Helfen L, Baumbach T, Johnson G, Spearing SM, et al. In situ synchrotron computed laminography of damage in carbon fibre-epoxy [90/0](s) laminates. *Scripta Mater*. 2010;62(2):97-100.
- [27] Morgenevener TF, Helfen L, Sinclair I, Proudphon H, Xu F, Baumbach T. Ductile crack initiation and propagation assessed via in situ synchrotron radiation-computed laminography. *Scripta Mater*. 2011;65(11):1010-3.
- [28] Xu F, Helfen L, Moffat AJ, Johnson G, Sinclair I, Baumbach T. Synchrotron radiation computed laminography for polymer composite failure studies. *J Synchrotron Radiat*. 2010;17:222-6.
- [29] Helfen L, Myagotin A, Mikulik P, Pernot P, Voropaev A, Elyyan M, et al. On the implementation of computed laminography using synchrotron radiation. *Rev Sci Instrum*. 2011;82(6).
- [30] Xu F, Helfen L, Baumbach T, Suhonen H. Comparison of image quality in computed laminography and tomography. *Opt Express*. 2012;20(2):794-806.
- [31] Sanchu-Saez S, Barbero E, Zaera R, Navarro C. Compression after impact of thin composite laminates. *Compos Sci Technol*. 2005;65(13):1911-9.
- [32] Shyr TW, Pan YH. Impact resistance and damage characteristics of composite laminates. *Compos Struct*. 2003;62(2):193-203.
- [33] Hull D, Shi YB. Damage Mechanism Characterization in Composite Damage Tolerance Investigations. *Compos Struct*. 1993;23(2):99-120.
- [34] Wright P, Moffat A, Sinclair I, Spearing SM. High resolution tomographic imaging and modelling of notch tip damage in a laminated composite. *Compos Sci Technol*. 2010;70(10):1444-52.
- [35] Groleau MR, Shi YB, Yee AF, Bertram JL, Sue HJ, Yang PC. Mode II fracture of composites interlayered with nylon particles. *Compos Sci Technol*. 1996;56(11):1223-40.
- [36] Sue HJ, Jones RE, Garciameitin EI. Fracture-Behavior of Model Toughened Composites under Mode-I and Mode-II Delaminations. *J Mater Sci*. 1993;28(23):6381-91.
- [37] Aksoy A, Carlsson LA. Interlaminar Shear Fracture of Interleaved Graphite Epoxy Composites. *Compos Sci Technol*. 1992;43(1):55-69.
- [38] Gregory JR, Spearing SM. Modeling inelastic matrix crack tip deformation in a double cantilever beam specimen. *J Compos Mater*. 2006;40(2):143-56.
- [39] Moffat AJ, Wright P, Buffiere JY, Sinclair I, Spearing SM. Micromechanisms of damage in 0 degrees splits in a [90/0](s) composite material using synchrotron radiation computed tomography. *Scripta Mater*. 2008;59(10):1043-6.
- [40] Shan Y, Liao K. Environmental fatigue behavior and life prediction of unidirectional glass-carbon/epoxy hybrid composites. *Int J Fatigue*. 2002;24(8):847-59.
- [41] Gamstedt EK, Talreja R. Fatigue damage mechanisms in unidirectional carbon-fibre-reinforced plastics. *J Mater Sci*. 1999;34(11):2535-46.

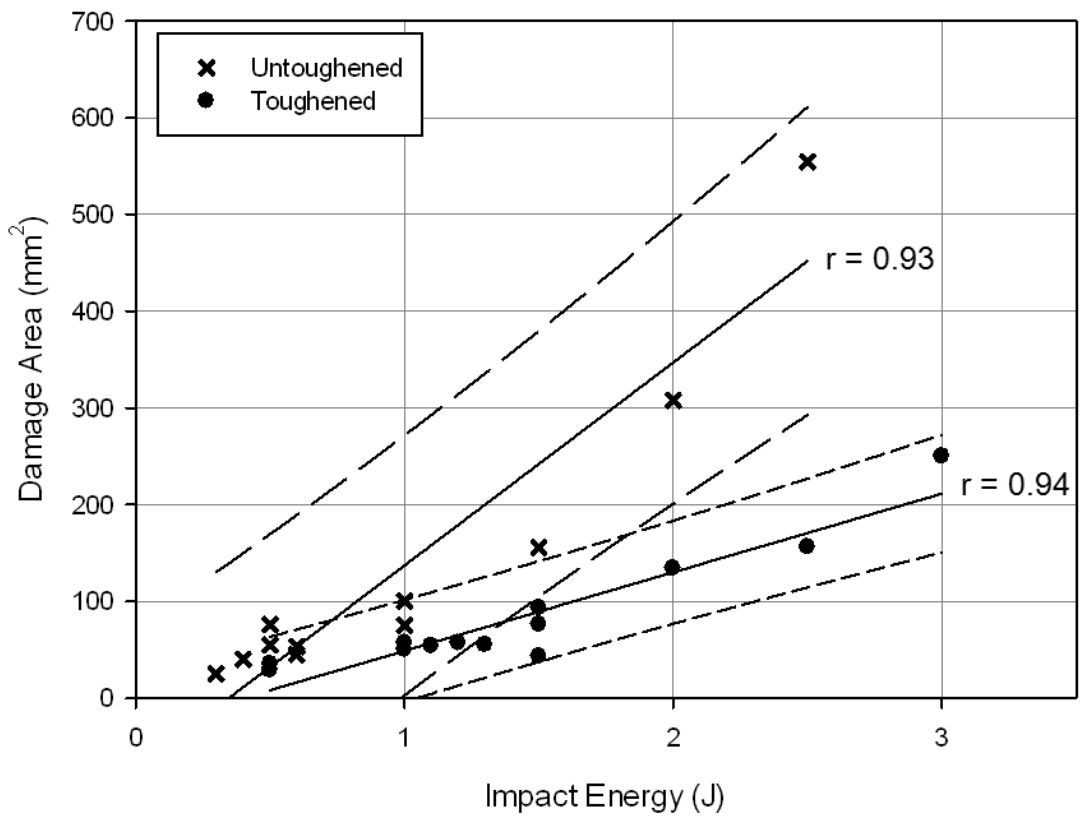


Figure 1 – Scatter plot of C-scan projected damage area vs. impact energy for untoughened and particle-toughened specimens. Linear fits are shown along with dashed lines representing 95% prediction intervals.

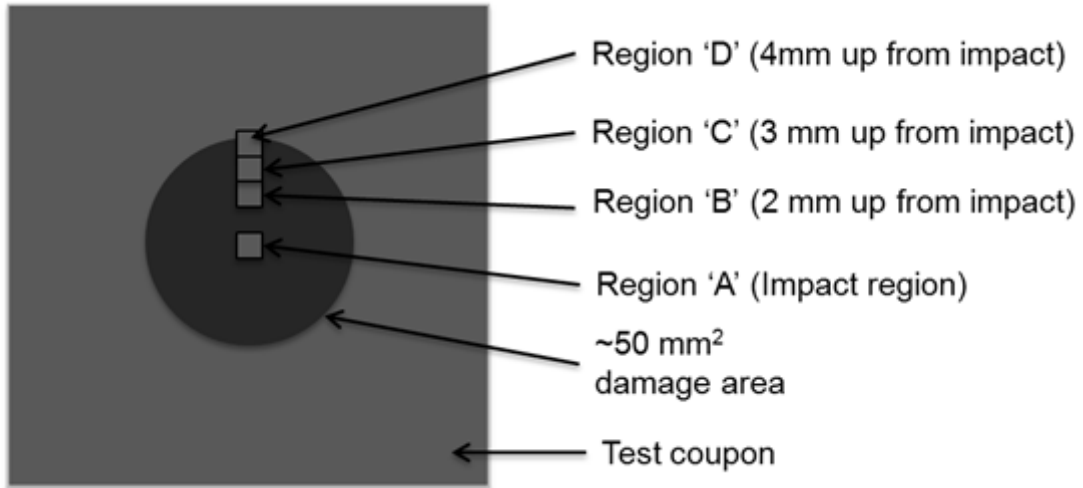


Figure 2 – Schematic showing the four SRCL local scanning locations undertaken for both the untoughened and toughened systems.

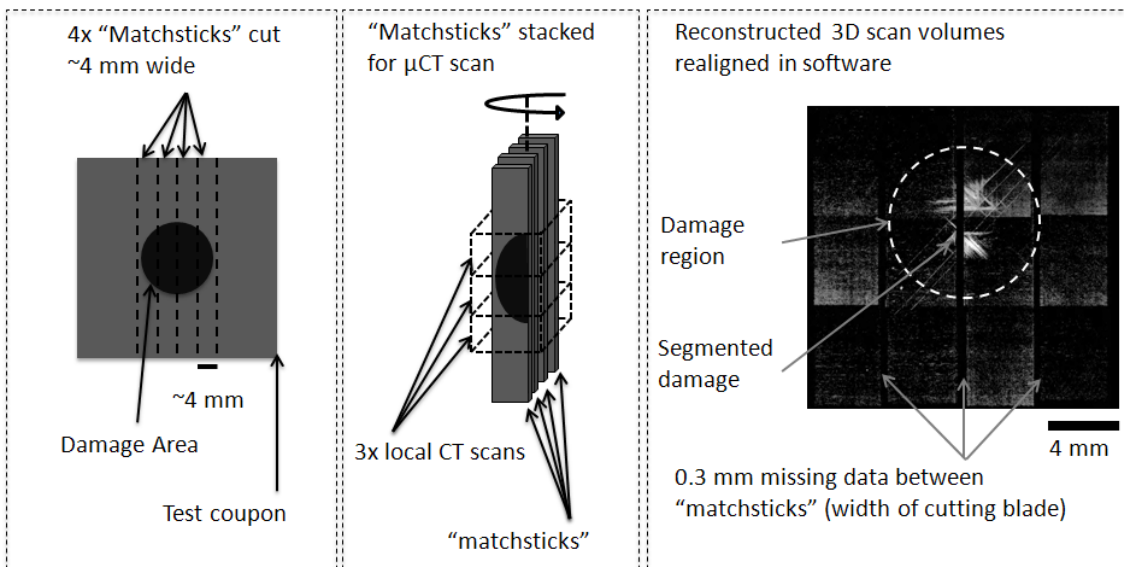


Figure 3 – Schematic showing coupons prepared for μCT scans and realignment.

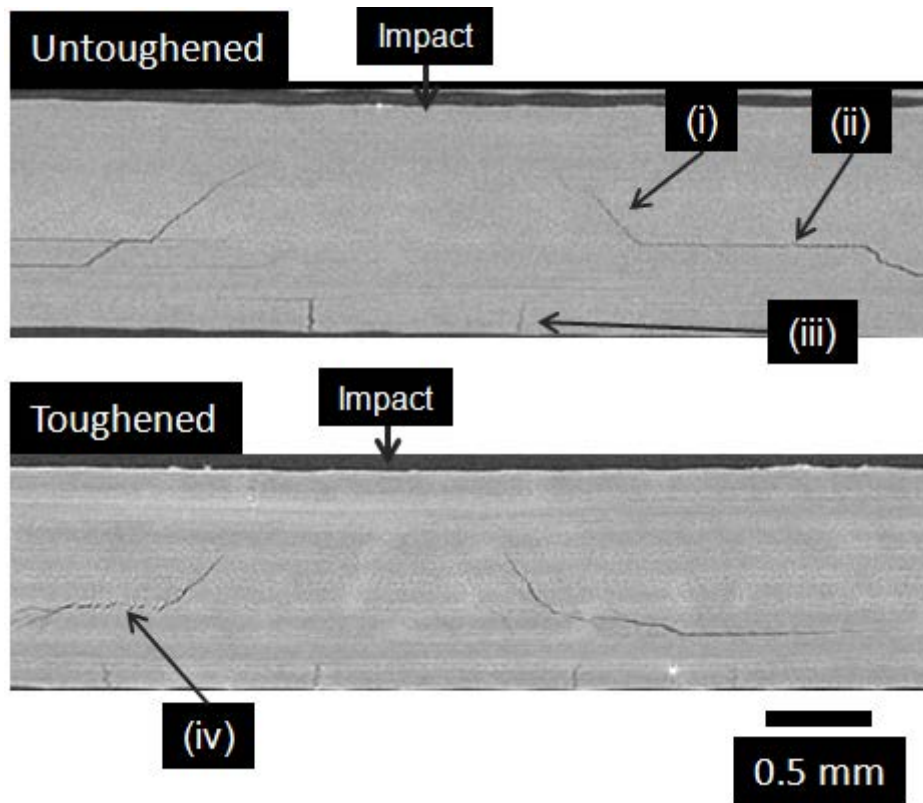


Figure 4 - μ CT 2D cross-section showing post-impact damage for untoughened (0.6J) and particle toughened (1.2J) systems. Typical damage modes are identified (i) matrix crack, (ii) delaminations, (iii) tensile cracks and (iv) cracks exhibiting ligamented behaviour.

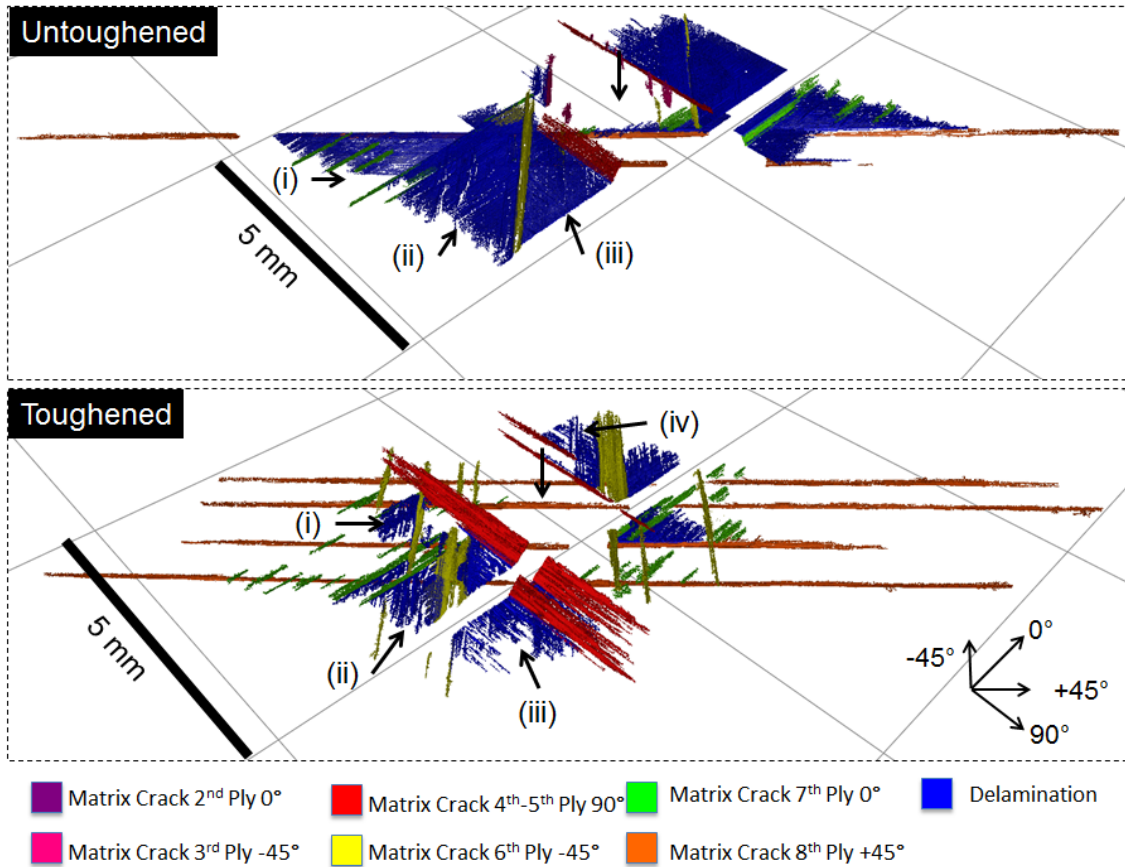


Figure 5 – μ CT 3D damage segmentation of impacted 8 ply coupons for (a) untoughened (0.6 J) and (b) particle-toughened material (1.2 J). Point of impact is indicated by the arrow and grid lines are spaced 5 mm apart. Colour version available online.

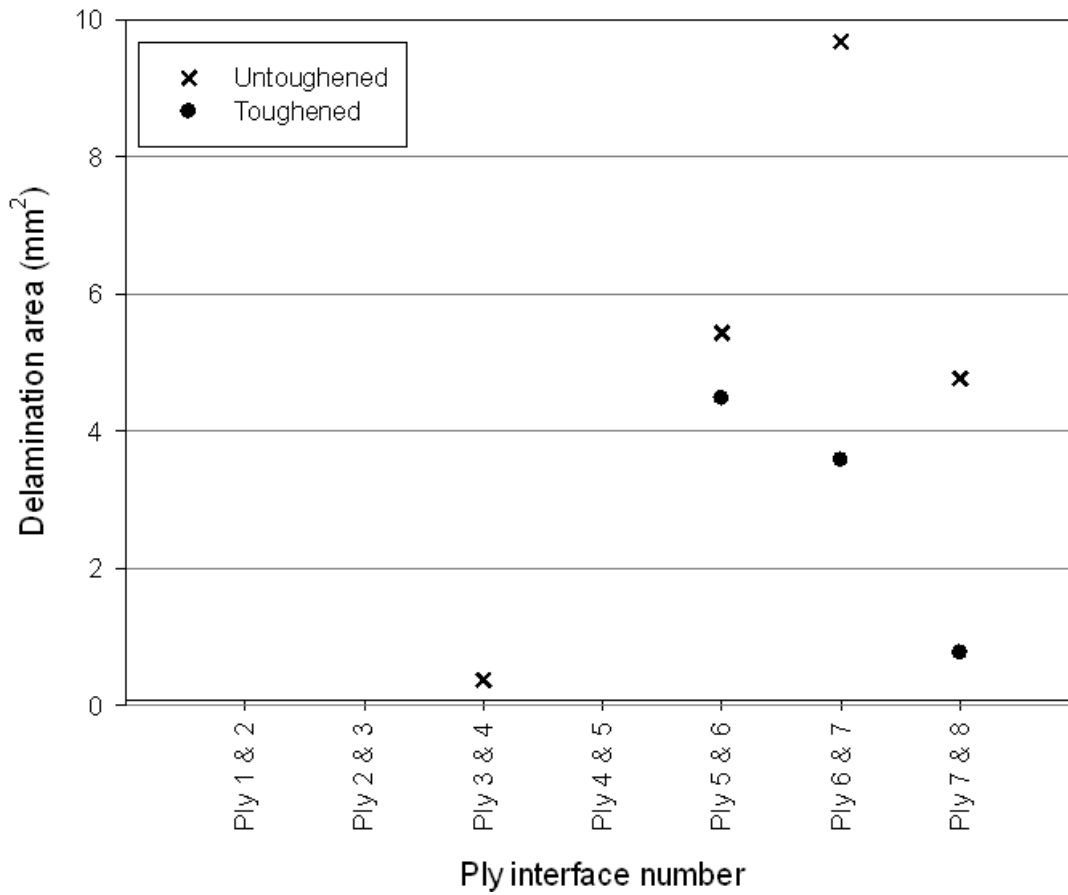


Figure 6 – Delamination areas measured at each ply interface for untoughened (0.6 J) and toughened (1.2 J) systems.

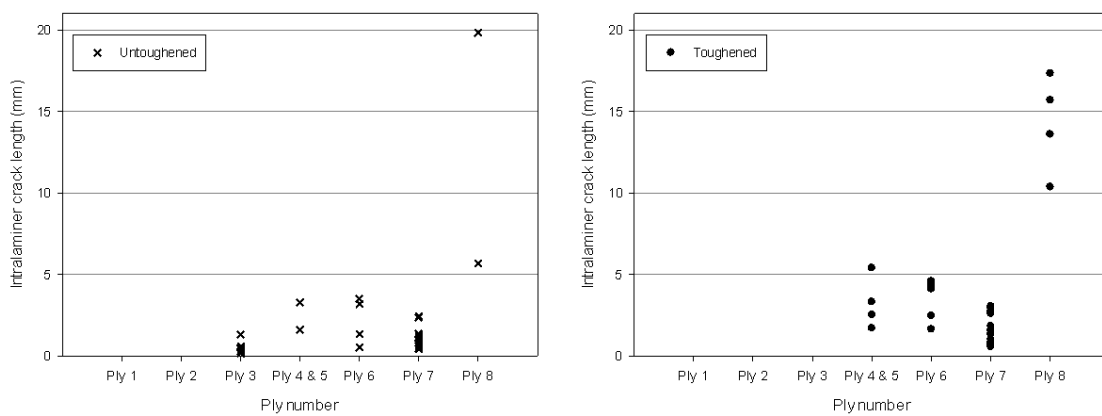


Figure 7 – Scatter plot of intralaminar matrix crack lengths on each ply measured from μ CT volumes on the untoughened (0.6 J) and toughened (1.2 J) systems. Ply 1 represents the impact side and ply 8 the back face.

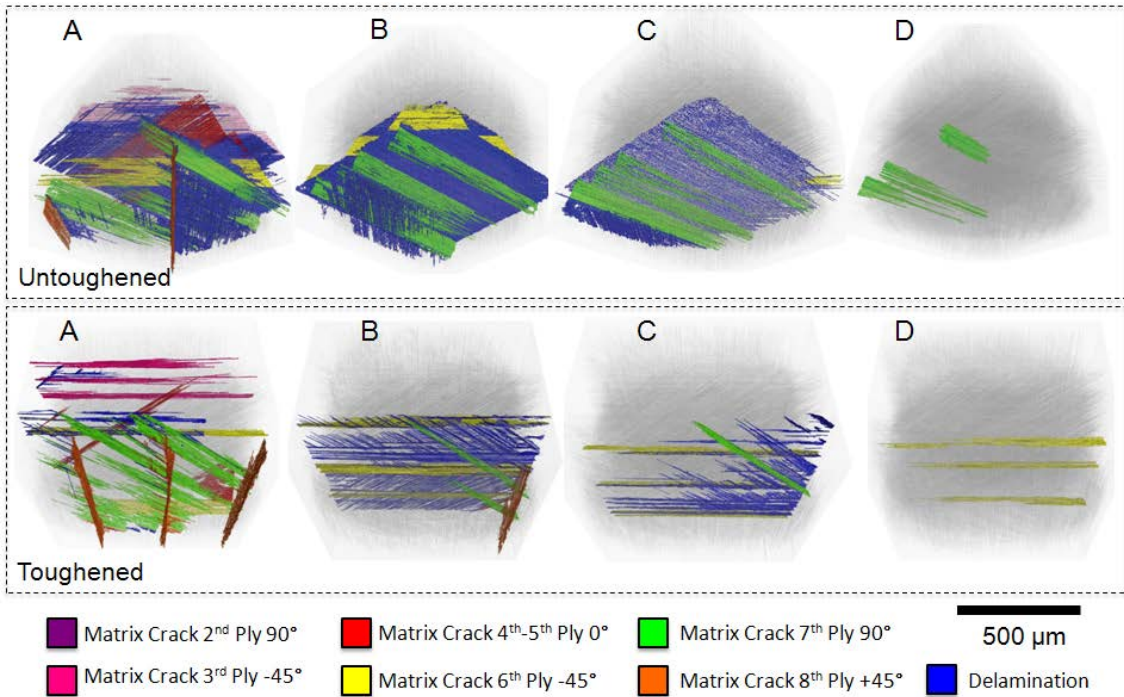


Figure 8 – 3D segmentations of interlaminar and intralaminar cracks from SRCL scans taken at region A to D for untoughened (0.6 J upper row), and toughened (1.2 J bottom row) systems.

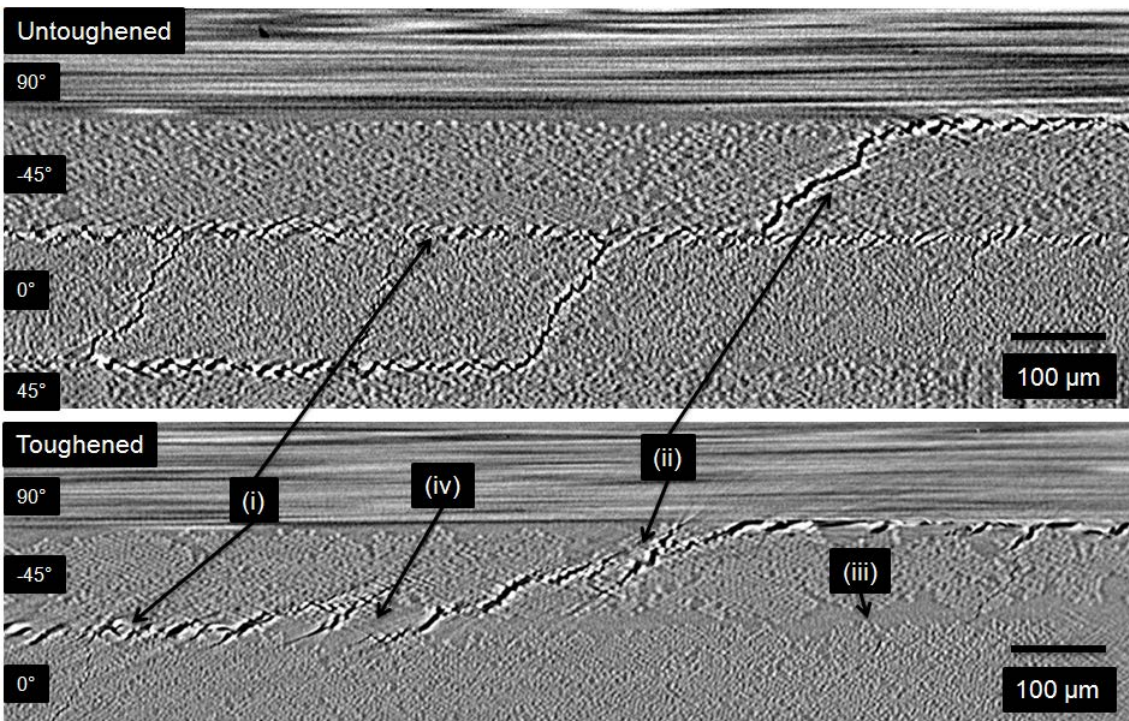


Figure 9 – SRCL cross-section of untoughened (0.6 J) and toughened (1.2 J) taken from Region 'B'. The image shows a region below the mid-plane at the same interface plies in both systems. (i) indicates delaminations, (ii) matrix crack, (iii) ~20 µm resin rich region and (iv) bridging ligaments.

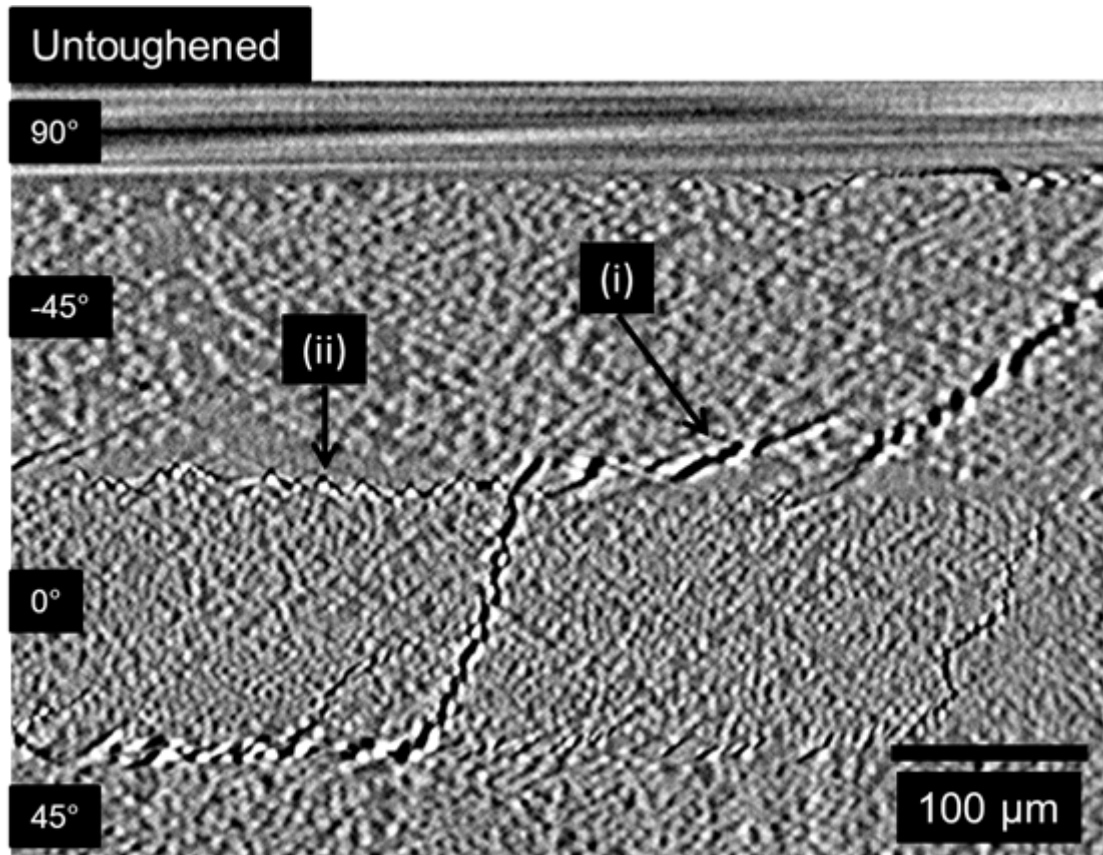


Figure 10 – SRCL cross-section taken from Region 'A' in the untoughened material system. Variation in resin thickness led to a rich region present in (i) leading to ligaments with similar characteristics to the toughened system. (ii) show microscopic fibre-resin debonding.

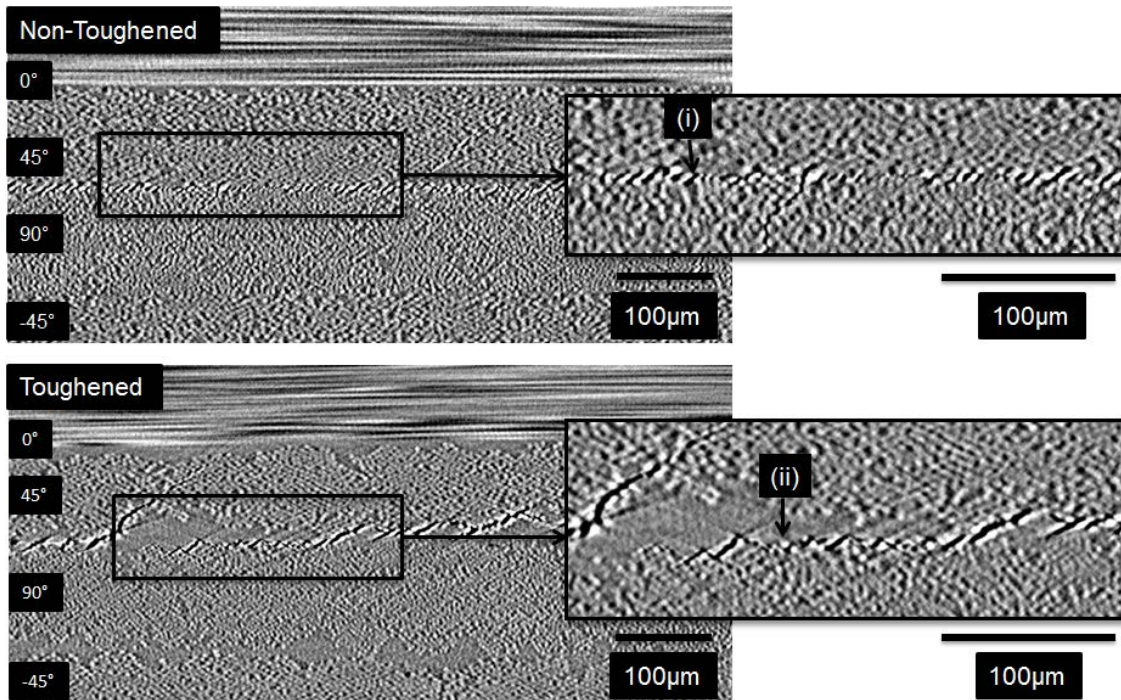


Figure 11 – SRCL cross-section taken from the edge of the damaged area in Region ‘C’. (i) crack deflection on the order of single fibre diameters and (ii) fibre-resin debonding .